Article

Neuron

Alpha-Beta and Gamma Rhythms Subserve Feedback and Feedforward Influences among Human Visual Cortical Areas

Highlights

- Gamma mediates forward and alpha-beta feedback influences among human visual areas
- Human inter-areal directed influences correlate with macaque laminar connectivity
- Rhythmic inter-areal influences establish a hierarchy of 26 human visual areas
- Alpha-beta influences differentially affect ventral- and dorsal-stream visual areas

Authors

Georgios Michalareas, Julien Vezoli, Stan van Pelt, Jan-Mathijs Schoffelen, Henry Kennedy, Pascal Fries

Correspondence

giorgos.michalareas@esi-frankfurt.de (G.M.), pascal.fries@esi-frankfurt.de (P.F.)

In Brief

Michalareas et al. show that in human visual cortex influences along feedforward projections predominate in the gamma band, whereas influences along feedback projections predominate in the alpha-beta band. These influences constrain a functional hierarchy in agreement with macaque anatomical hierarchy.

Michalareas et al., 2016, Neuron *89*, 384–397
January 20, 2016
http://dx.doi.org/10.1016/j.neuron.2015.12.018

CellPress

CellPress

Neuron
Article

Alpha-Beta and Gamma Rhythms Subserve Feedback and Feedforward Influences among Human Visual Cortical Areas

Georgios Michalareas,[1,*] Julien Vezoli,[1] Stan van Pelt,[1,2] Jan-Mathijs Schoffelen,[2,3] Henry Kennedy,[4,5] and Pascal Fries[1,2,*]

[1]Ernst Strüngmann Institute (ESI) for Neuroscience in Cooperation with Max Planck Society, Deutschordenstraße 46, 60528 Frankfurt, Germany

[2]Donders Institute for Brain, Cognition and Behaviour, Radboud University Nijmegen, Kapittelweg 29, 6525 EN Nijmegen, the Netherlands

[3]Max Planck Institute for Psycholinguistics, Wundtlaan 1, 6525 XD Nijmegen, the Netherlands

[4]Stem Cell and Brain Research Institute, INSERM U846, 18 Avenue Doyen Lépine, 69675 Bron, France

[5]Université de Lyon, 37 Rue du Repos, 69361 Lyon, France

*Correspondence: giorgos.michalareas@esi-frankfurt.de (G.M.), pascal.fries@esi-frankfurt.de (P.F.)

http://dx.doi.org/10.1016/j.neuron.2015.12.018

SUMMARY

Primate visual cortex is hierarchically organized. Bottom-up and top-down influences are exerted through distinct frequency channels, as was recently revealed in macaques by correlating inter-areal influences with laminar anatomical projection patterns. Because this anatomical data cannot be obtained in human subjects, we selected seven homologous macaque and human visual areas, and we correlated the macaque laminar projection patterns to human inter-areal directed influences as measured with magnetoencephalography. We show that influences along feedforward projections predominate in the gamma band, whereas influences along feedback projections predominate in the alpha-beta band. Rhythmic inter-areal influences constrain a functional hierarchy of the seven homologous human visual areas that is in close agreement with the respective macaque anatomical hierarchy. Rhythmic influences allow an extension of the hierarchy to 26 human visual areas including uniquely human brain areas. Hierarchical levels of ventral- and dorsal-stream visual areas are differentially affected by inter-areal influences in the alpha-beta band.

INTRODUCTION

Non-human primate visual cortical areas are organized in a hierarchy with characteristic laminar patterns of feedforward and feedback projections (Felleman and Van Essen, 1991; Barone et al., 2000; Markov et al., 2014). Feedforward projections typically target layer 4. They originate predominantly from superficial layers, and this predominance increases with the number of hierarchical levels bridged by the projection. By contrast, feedback projections typically target layers 1 and 6. They originate predominantly from infragranular layers, and this predominance increases with the number of hierarchical levels bridged by the projection. In agreement with this, contextual feedback signals activate predominantly superficial layers in human V1 (Olman et al., 2012; Muckli et al., 2015).

Cortical layers differ not only in their projection patterns, but also with regard to local rhythmic synchronization. Synchronization in the gamma frequency band is strongest in superficial layers, whereas synchronization in the alpha-beta frequency band is strongest in infragranular layers (Buffalo et al., 2011; Xing et al., 2012). These results, taken together with the laminar projection patterns, suggest that gamma might subserve feedforward and alpha-beta feedback signaling (Lee et al., 2013; Fries, 2015). This is supported by patterns of inter-laminar delay and causality (Livingstone, 1996; Bollimunta et al., 2008; Plomp et al., 2014). Further, electrical stimulation of V1 induces enhanced gamma-band activity in V4, whereas area V4 stimulation induces enhanced alpha-beta-band activity in V1 (van Kerkoerle et al., 2014).

When directed inter-areal influences across 28 area pairs are assessed through large-scale high-density electrocorticography in rhesus macaques and correlated with anatomical projection patterns, gamma is found systematically stronger in the feedforward direction and beta in the feedback direction (Bastos et al., 2015). The high consistency of this effect made it possible to construct a hierarchy of visual areas based on directed influences alone. These findings raise the intriguing possibility that a similar analysis in human cortex would reveal the functional hierarchy of visual areas. In human subjects, anatomical tract tracing methods, requiring active axonal transport, are neither possible in the living nor in the post-mortem brain. Further, tractographic analysis of diffusion MRI does not indicate the directionality of pathways and therefore cannot explore the hierarchical organization of inter-areal pathways.

In the present study, we have first selected seven human areas showing strong homology to macaque areas. This enabled us to infer the structural hierarchy in the human cortex and to examine its functional hierarchy using magnetoencephalography (MEG). This shows that causal interactions along the feedforward and feedback pathways are exerted in distinct frequency bands.

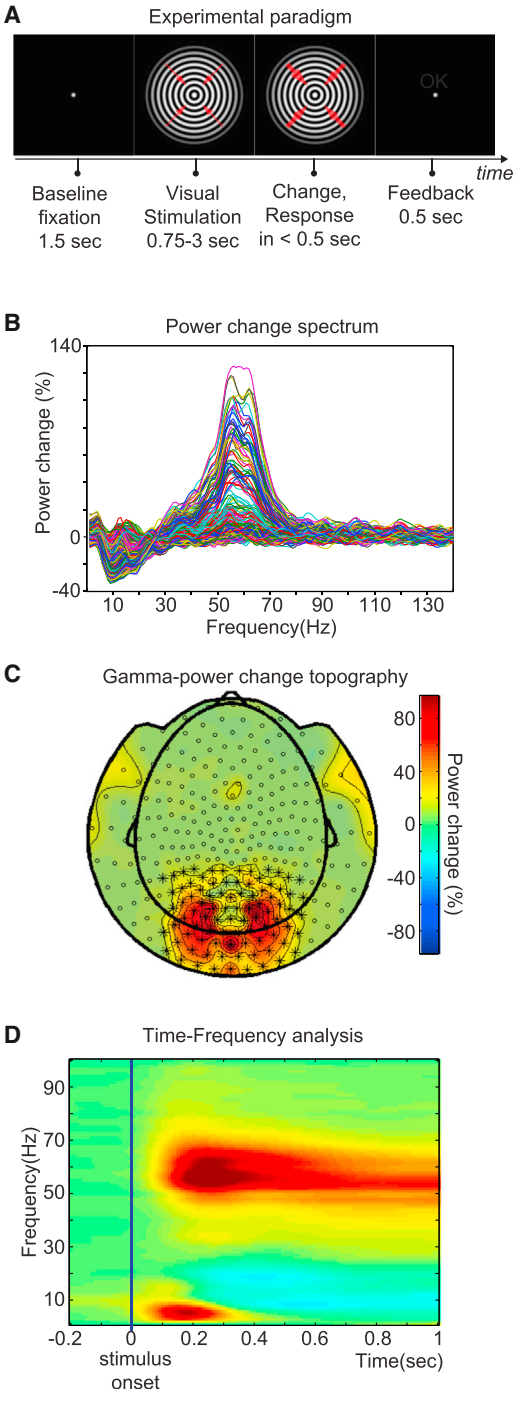

Figure 1. Experimental Paradigm and Visually Induced Changes in MEG Signal Power in Frequency, Space, and Time

(A) Experimental paradigm. The fixation period was followed by the presentation of a circular sine-wave grating, centered at the fixation point and contracting toward its center. At a random moment between 0.75 and 3 s after stimulus onset, velocity increased, which was reported by the subjects with their right index finger. Thicker red arrows indicate the speed change.

(B) Spectrum of power change during stimulation versus baseline (−0.5 to −0.2 s). Each line represents the average across subjects for one MEG sensor.

(C) Sensor-level topography of power change from (B) in the frequency range of 40 to 75 Hz.

(D) Average power change as a function of time and frequency for selected sensors over occipito-parietal areas, shown with * in (C). Color bar applies to (C) and (D).

Based on these functional markers, we were able to derive the full hierarchy of 26 human visual areas based on the asymmetry of their feedforward and feedback interactions.

RESULTS

Visually Induced Responses

Forty-three human subjects were instructed to attentively monitor a visual stimulus for unpredictable changes, in order to engage both bottom-up and top-down influences. This paradigm reliably induces gamma-band activity in visual cortex (Hoogenboom et al., 2006). While subjects fixated centrally, a large circular sine-wave grating contracting toward the fixation point was presented. The stimulus could change speed at any time between 0.75 and 3 s after onset, which had to be reported within 0.5 s in order to obtain positive feedback (Figure 1A). Visual stimulation and task performance induced grand-average power reductions in the alpha and beta bands and enhancements in the gamma band in many sensors (Figure 1B), consistent with previous reports (Hoogenboom et al., 2006; van Pelt et al., 2012). Gamma power enhancements were strongest over occipital and parietal MEG sensors (Figure 1C). The sensors marked in Figure 1C show stimulus-induced gamma power enhancements that start around 0.1 s after stimulus onset and are sustained for the duration of visual stimulation and task performance (Figure 1D). Alpha and beta power shows sustained reductions at a slightly longer latency. Between 0.05 and 0.35 s, there is an additional theta (3–8 Hz) power enhancement, most likely reflecting the event-related field (ERF) (Jutai et al., 1984). To avoid the ERF and the effect of its non-stationarity on Granger causality (GC) estimation (Wang et al., 2008), further analyses use the data from 0.365 s after stimulus onset up to the stimulus change, segmented into non-overlapping 0.365 s epochs (see Experimental Procedures).

Induced gamma power change estimated at the level of the cortical sheet revealed an occipital peak extending into parietal and temporal regions (Figure 2A). In order to investigate GC among human visual areas and to compare it to macaque laminar connectivity, we selected seven visual areas, for which anatomical retrograde tracing data were available, and for which there is evidence of inter-species homology (see Experimental Procedures). These areas and their homologies are illustrated in Figure 2B. Areas V1 and V2 are substantially larger than any one of the other areas (Figure 2B) and exhibit the largest gamma power enhancements (Figure 2A). To render V1 and V2 more comparable in size to the other areas, and to focus on their visually activated subregions, we used the vertices inside V1 and V2 that were within 2 cm from the local gamma maxima. These vertices and the vertices of the remaining areas are shown in Figure 2C.

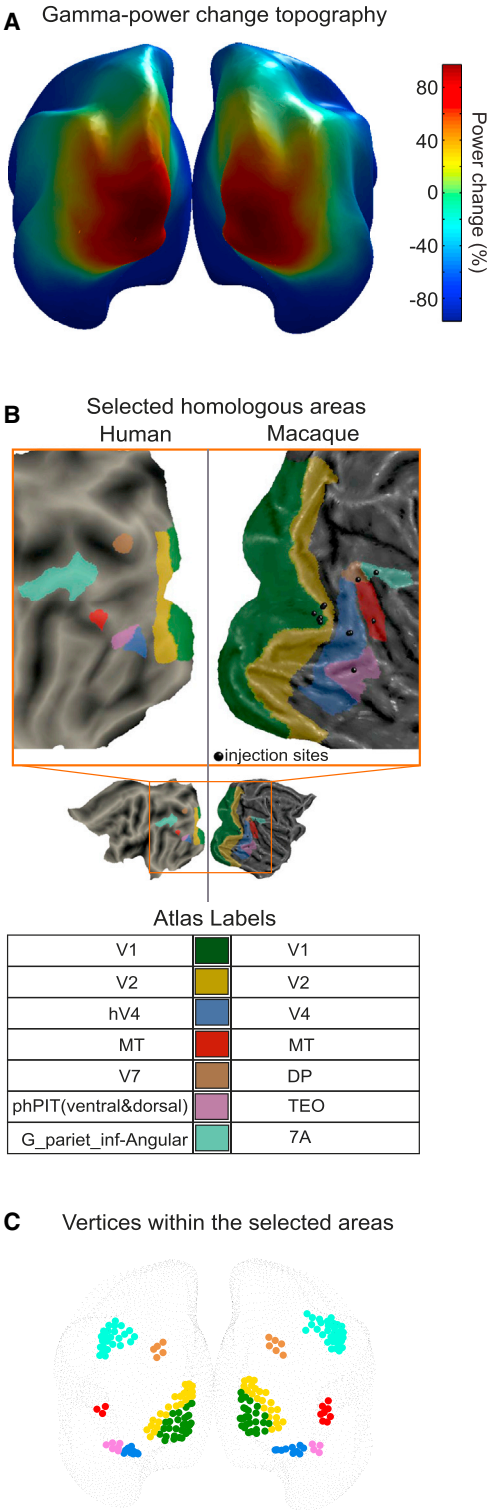

Figure 2. Gamma Power Distribution on the Cortical Sheet and Human-Macaque Homology Definition

(A) Gamma-power change distribution on the cortical sheet as derived from inverse solution.

(B) Selected human-macaque homologous visual areas. Displayed on flat cortical maps. The small black spheres on the macaque flat cortex indicate the injection sites of retrograde tracer published in Markov et al. (2014).

(C) Vertices representing the human homologous areas from (B) in the MEG inverse solution on the very inflated Conte69 template brain.

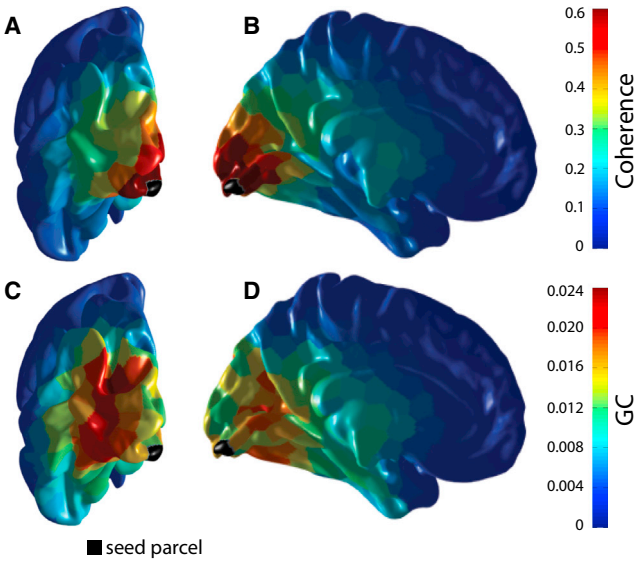

Figure 3. GC Limits the Effect of Field Spread

(A–D) For this investigation, each hemisphere was randomly segmented into 400 parcels according to the fast marching algorithm (Sethian, 1999). There were on average ten vertices per parcel. The parcel closest to the peak of the average gamma power over all subjects was identified and was selected as the seed parcel, marked here in black.

(A and B) Coherence was computed for each subject between this seed parcel and the remaining 399 parcels. These coherence values were subsequently averaged across all subjects for each pair and each frequency. Finally, for each pair, the coherence values within the gamma band (40 to 75 Hz) were averaged.

(C and D) GC from the seed to the rest of the parcels for the same frequency range.

GC—Field Spread Effect

MEG sensors pick up mixtures of signals from multiple sources in the brain. This mixing can be partly deciphered by projecting MEG data into source space. However, the closer two estimated sources are, the larger the remaining mixing, an effect referred to as "field spread" (Schoffelen and Gross, 2009). Field spread leads to artifactual correlation or coherence for source signals from proximate locations. Because field spread decays with distance between sources, the dominant spatial pattern of coherence to a given source (the black parcel in Figure 3) is a smooth decay with distance from that source (Figures 3A and 3B). By contrast, the spatial pattern of GC exerted by that source does not show this smooth decay, but rather, it shows spatial peaks that have their maximum not at the source or in the immediate vicinity of the source (Figures 3C and 3D). This is likely due to the fact that field spread is instantaneous. GC eliminates instantaneous correlations because they are not indicative of a causal influence.

GC in Feedforward and Feedback Directions

GC was computed between all possible pairs of the seven selected visual areas. In order to estimate bias due to the GC metric used and the finite sample size, data epochs were randomized at each source location and GC computation was repeated. This bias estimation also entails an estimate of residual stimulus-locked components remaining after exclusion of the first 0.365 s after stimulus onset. The two hemispheres were analyzed independently.

We averaged all inter-areal GC spectra and compared them to the average bias estimate in order to obtain a first estimate of overall inter-areal GC, in particular for the main spectral peaks, (Figure 4A). Average inter-areal GC exceeded the bias estimate across the spectrum and showed two clear peaks: one in the alpha-beta range, peaking at 11 Hz, and one in the gamma band, peaking around 60 Hz. Previous studies have shown clear differences between alpha and beta rhythms (Wang, 2010; Bressler and Richter, 2015; Haegens et al., 2014; Gregoriou et al., 2015); however, the present analysis revealed one peak spanning across alpha and beta frequency ranges (similar to Buffalo et al., 2011), which we therefore refer to as the alpha-beta band. Peak frequencies were essentially identical in the two hemispheres.

We used macaque laminar connectivity data that quantifies the degree to which a given inter-areal projection has a feedforward or feedback character in order to investigate whether GC differed between the feedforward and feedback directions. Retrograde tracer injection into a target area leads to labeling of projection neurons in the source areas. The more pronounced the feedforward (feedback) character of the anatomical projection, the higher (lower) is the proportion of supragranular projection neurons (Barone et al., 2000; Markov et al., 2014). This anatomical signature of the feedforward or feedback character of a projection is captured by the supragranular labeled neuron (SLN) index, i.e., the number of supragranular labeled neurons divided by the sum of supragranular and infragranular labeled neurons.

The SLN value for all projections among the seven selected macaque visual areas was calculated (Markov et al., 2014). If, between area A and area B, the SLN for the A-to-B projection was higher than the SLN for the B-to-A projection, then A-to-B was considered a feedforward and B-to-A a feedback projection. GC values were averaged independently for both directions in each area pair (Figures 4B and 4C for the left and right hemispheres, respectively). The same was done with the surrogate data in order to estimate bias. GC significantly exceeded the bias estimate across the entire spectrum. GC in the alpha-beta band was stronger in feedback than in feedforward directions. In contrast, GC in the gamma band was substantially stronger in feedforward than in feedback directions. The statistical comparison revealed significant differences exclusively in these two frequency bands. Results are very similar in both hemispheres. The alpha-beta band cluster ($p < 0.05$) ranged from 7 to 17 Hz in both hemispheres. The gamma-band cluster ($p < 0.05$) ranged from 42 to 93 Hz in the left hemisphere and from 41 to 84 Hz in the right hemisphere.

Figure 4D shows the GC in feedforward and feedback directions for all area pairs. GC peaks in the gamma and alpha-beta bands for all area pairs of both hemispheres. For all area pairs, GC exceeded the bias estimate for frequencies up to the upper end of the gamma band. When GC is compared between feedforward and feedback directions, most area pairs confirm the above pattern. The results for the alpha-beta band are as follows: In the left hemisphere, alpha-beta GC was stronger in the feedback than in the feedforward direction in 13 out of 21 area pairs (61.91%), weaker in 1 area pair (MT-TEO; 4.76%), and not significantly different in another 7 (33.33%); i.e., it was more frequently significantly stronger in the feedback than in the feedforward direction ($p = 0.0018$, sign test here and for the following tests). In the right hemisphere, alpha-beta GC was stronger in the feedback than in the feedforward direction in 13 out of 21 area pairs (61.91%), weaker in 2 area pairs (MT-TEO and MT-DP; 9.52%), and not significantly different in another 6 (28.57%) ($p = 0.0074$). The results for the gamma band are as follows: In the left hemisphere, gamma GC was stronger in the feedforward than in the feedback direction in 17 out of 21 area pairs (80.95%), weaker in 1 area pair (DP-7A; 4.76%), and not significantly different in 3 other pairs (14.29%); i.e., it was more frequently significantly stronger in the feedforward than in the feedback direction ($p = 0.00015$). In the right hemisphere, gamma GC was stronger in the feedforward than in the feedback direction in 16 out of 21 area pairs (76.19%), weaker in 1 area pair (DP-7A; 4.76%), and not significantly different in 4 other pairs (19.05%) ($p = 0.00028$).

The peak in the GC spectra that we have identified as the alpha-beta peak spans the classical alpha- and beta-frequency bands. Alpha- and beta-band rhythms vary in frequency across subjects and can be influenced by stimulus and task conditions (Haegens et al., 2014). We calculated the average inter-areal GC among the seven visual areas separately per subject. When Gaussians were fitted to these averages in the 4–20 Hz range, most alpha-beta peaks were well approximated by a single Gaussian and the resulting peak frequencies extended from 7 to 19 Hz (Figures S1A and S1B; mean ± SD = 11.02 ± 2.45 Hz). Likewise, when Gaussians were fitted to the GC averages in the 30–100 Hz range, the resulting gamma peak frequencies extended from 52 to 69 Hz (Figures S1C and S1D; mean ± SD = 59.16 ± 4.16 Hz). Similar cross-subject variability has been described in previous studies using the same stimulus and task as used here and has been related to genetic factors (Hoogenboom et al., 2006; van Pelt et al., 2012). To account for this inter-subject variability in peak frequencies, we repeated the above GC analyses after aligning alpha-beta and gamma peak frequencies, respectively, across subjects (Figure 5). After alignment, GC values tended to increase, and the above differences between GC in the feedforward and feedback direction were confirmed. Significant differences remained identical except in a few cases, the most notable being V1 and V2 in the right hemisphere, changing from an insignificant difference to a stronger alpha-beta GC in the feedforward than in the feedback direction.

Because the peak-aligned analysis accounts for inter-subject variability, it was used for all further analyses (results without peak alignment are provided as supplemental information and are qualitatively identical).

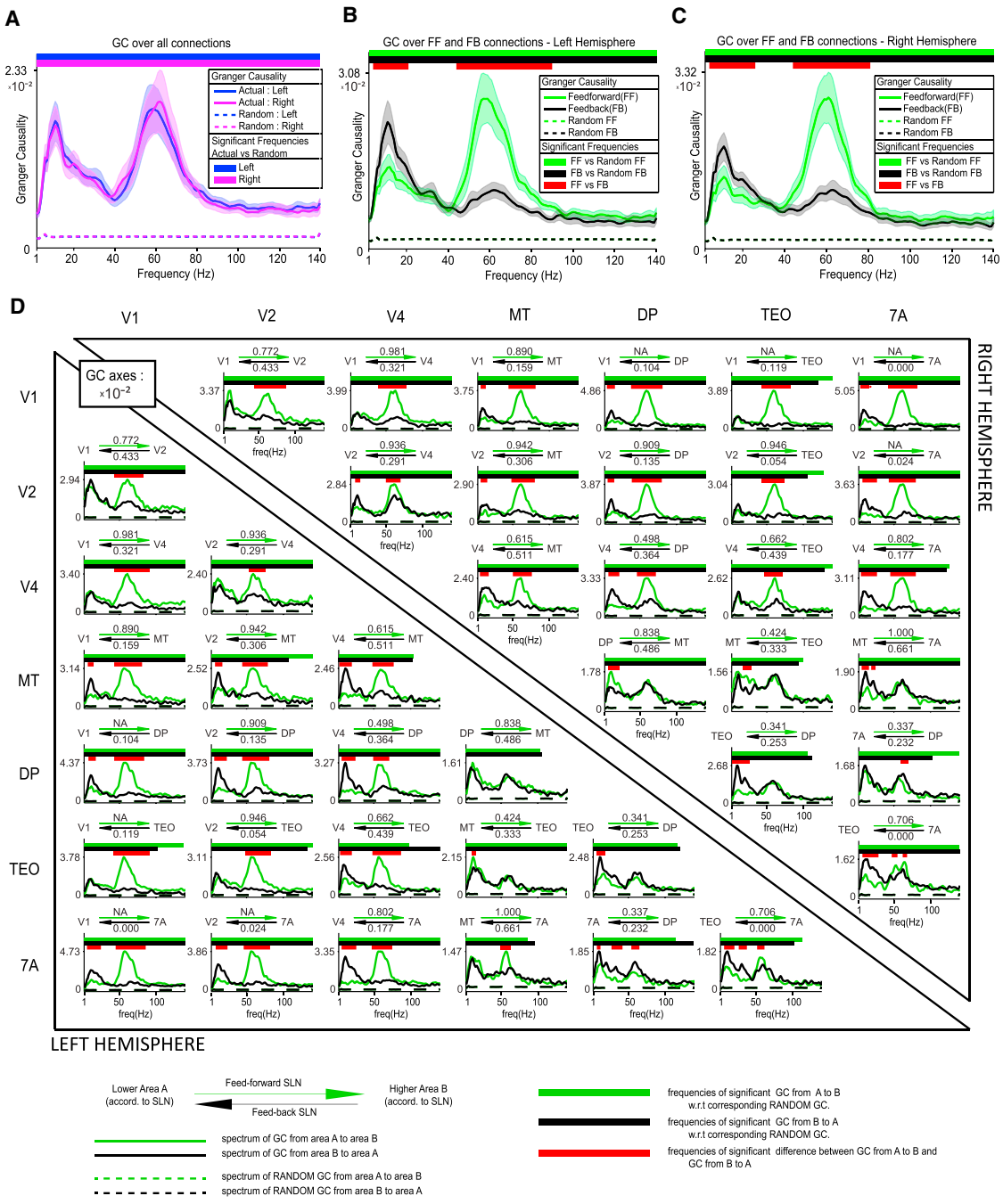

Figure 4. GC in Feedforward and Feedback Directions

(A) GC spectrum averaged across all pairs of areas. GC values were averaged across all area pairs and subjects, separately per hemisphere. Significance relative to the surrogate (random) data was computed by comparing for all subjects the GC between the original and the surrogate conditions using a permutation-based non-parametric statistical test.

(B and C) GC spectra averaged separately for inter-areal influences corresponding to feedforward (green) or feedback (black) projections. Two non-parametric statistical tests were performed: one between the actual and surrogate average GC spectra and one between the feedforward and feedback average GC spectra. This analysis was performed separately for the (B) left and (C) right hemispheres.

(D) GC spectra, averaged over subjects, separately per area pair and hemisphere. Again two non-parametric statistical tests were performed for each area pair: one between the actual and surrogate data and one between the feedforward and feedback direction. Tests were corrected for multiple comparisons across frequencies and across area pairs within each hemisphere. Left (right) hemisphere data are shown in the lower (upper) triangle. The two arrows above each subplot signify the feedforward (green arrow) and feedback (black arrow) characteristic of the anatomical projections, as defined by the anatomical SLN values (listed above and below the arrows). GC spectra in the feedforward direction are shown in green, and GC spectra in the feedback direction are shown in black. See information at the bottom of the plot for details on each subplot.

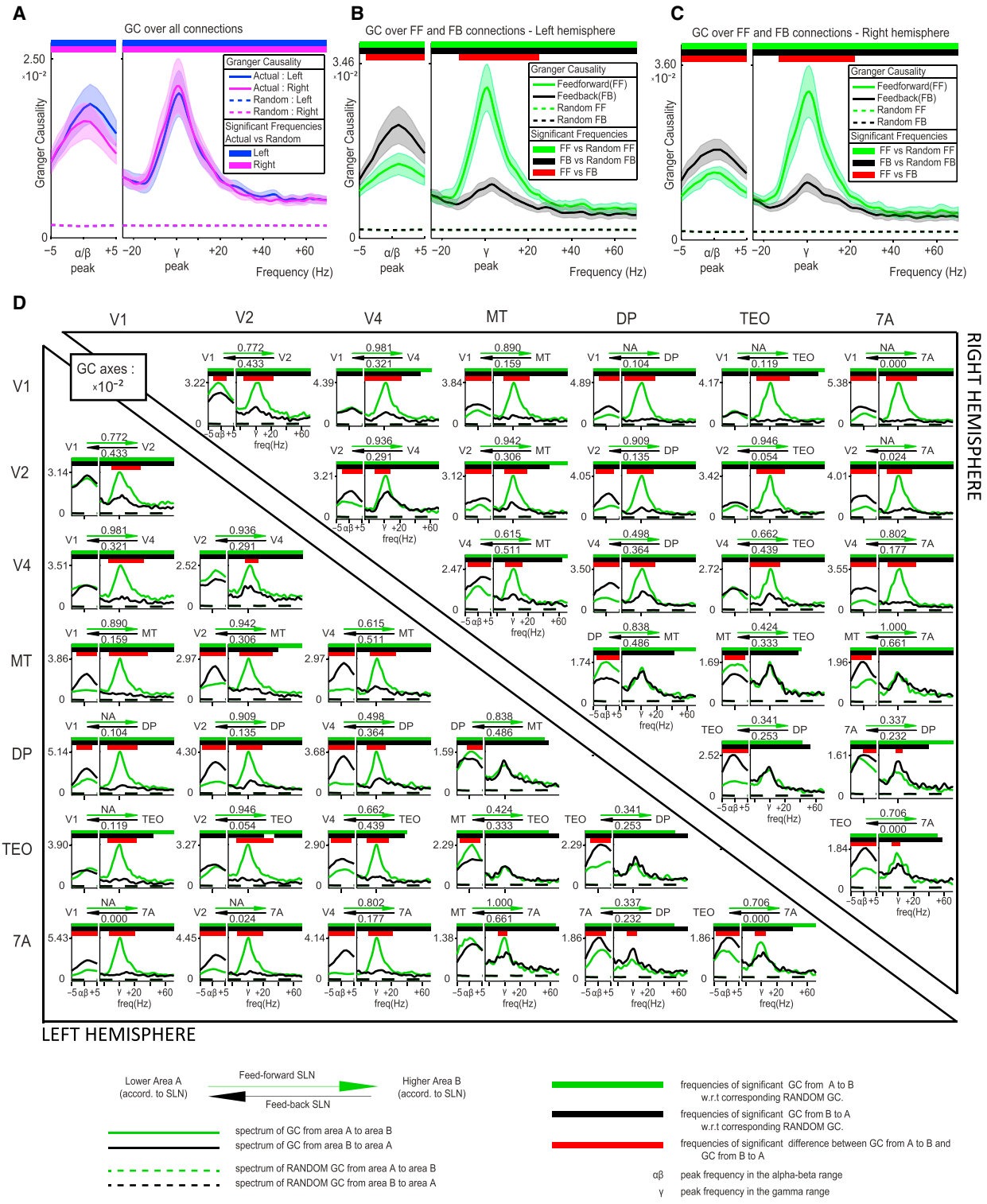

Figure 5. GC in Feedforward and Feedback Directions after Peak Alignment

(A–D) In order to account for inter-subject variability, two new frequency axes were devised, aligned to the individual alpha-beta and gamma peaks. The alpha-beta frequency axis spanned from −5 to +5 Hz around the alpha-beta peak. The gamma frequency axis spanned from −25 to +70 around the gamma peak. There was no overlap between these two frequency ranges for any subject. Otherwise, the analyses and figure format are the same as in Figure 4. (A) GC spectrum averaged across all pairs of areas. (B and C) GC spectra averaged separately for inter-areal influences corresponding to feedforward (green) or feedback (black) projections. This analysis was performed separately for the left (B) and right (C) hemispheres. (D) GC spectra, averaged over subjects, separately per area pair and hemisphere.

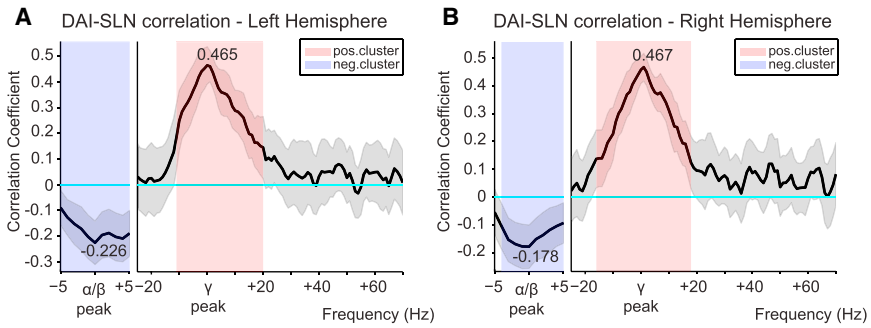

Figure 6. DAI-SLN Correlation Spectra Reveal Systematic Relation between GC and Anatomy

(A and B) Spearman correlation between DAI values (from human MEG) and SLN values (from macaque retrograde tracing) across pairs of visual areas. The DAI-SLN correlation was determined per frequency of the GC spectrum. The significance relative to zero was computed using a permutation-based non-parametric statistical test against the null hypothesis of zero correlation, with cluster-based multiple comparison correction. This analysis was performed separately for the (A) left and (B) right hemispheres. In both cases, a frequency cluster of negative correlation was identified in the alpha-beta range and a cluster of positive correlation was identified in the gamma range.

Correlation between Human Inter-areal GC and Macaque Anatomical Projections

So far, we have used the SLN metric to decide for each area pair, which one of the two reciprocal projections is feedforward and which one is feedback. As explained above, the SLN of an anatomical projection is the number of supragranular neurons normalized by the number of supragranular and infragranular neurons that give rise to the projection. Thus, the SLN quantifies the feedforward or feedback character of a projection in a graded metric. We next wanted to correlate this graded anatomical metric with a similarly graded functional metric, which captures the above-mentioned GC asymmetries. Therefore, we defined, as in Bastos et al. (2015), the directed influence asymmetry index (DAI) between areas A and B as

$$\mathrm{DAI}(\mathrm{A}-\mathrm{to}-\mathrm{B}) = (\mathrm{GC}(\mathrm{A}-\mathrm{to}-\mathrm{B}) - \mathrm{GC}(\mathrm{B}-\mathrm{to}-\mathrm{A}))/ (\mathrm{GC}(\mathrm{A}-\mathrm{to}-\mathrm{B}) + \mathrm{GC}(\mathrm{B}-\mathrm{to}-\mathrm{A})).$$

The numerator captures the predominant or net direction of GC, whereas the denominator provides a normalization factor such that the asymmetry in causal interactions can be compared between different area pairs and between different frequencies, for which raw GC values can differ substantially. Note that DAI is defined per frequency of the GC spectrum.

To test whether the GC asymmetry is systematically related to the feedforward-feedback character of the anatomical projections, we calculated the Spearman correlation coefficient between DAI values (from human MEG data) and SLN values (from macaque retrograde tracing data) across all visual area pairs. The seven visual areas under consideration give rise to 42 pairs, of which 38 had anatomical data that reached the threshold (i.e., more than ten labeled neurons). The DAI-SLN correlation was determined per GC frequency and per subject. Figure 6 shows the mean and SEM across the 43 subjects. The results for the left (Figure 6A) and right (Figure 6B) hemisphere were qualitatively identical. Also, the results remained qualitatively unchanged when the analysis was repeated without alignment to the subject-wise alpha-beta- and gamma-band peak frequencies (Figure S2).

Feedforward (feedback) anatomical projections predominantly originate in supragranular (infragranular) layers and are therefore characterized by a large (small) SLN (supragranular labeled neuron proportion), typically above (below) 0.5. Correspondingly, when the correlation is calculated between SLN values and DAI values, a positive DAI-SLN correlation for a given frequency range indicates that this frequency is systematically stronger (weaker) in the direction of feedforward (feedback) projections. Thus, the significant positive DAI-SLN correlation for the gamma band indicates that the net influence in this frequency is feedforward (left [right] hemisphere: mean = 0.465 [0.467], p = 0.0019 [0.0019]). The significant negative correlation for the alpha-beta band indicates that the net influence is feedback (left [right] hemisphere: mean = −0.226 [−0.178], p = 0.0159 [0.0139]).

A GC-Based Hierarchy Correlates with the Anatomical Hierarchy

SLN values have been used to establish an anatomical hierarchy of primate visual areas (Markov et al., 2014). In this hierarchy, the feedforward-feedback character of most inter-areal projections is in conformity with a global hierarchy, in which each area occupies a particular hierarchical level. For example, if the A-to-B projection is feedforward and the B-to-C projection is feedforward, then the A-to-C projection is typically strongly feedforward. Note there is no a-priori reason that prevents the A-to-C projection from being feedback, because neurons in A projecting to B and C are typically almost completely non-overlapping (Salin and Bullier, 1995) and neurons are exclusively either feedback or feedforward (Markov et al., 2014). The fact that inter-areal projections tend to confirm to a global hierarchy is an empirical finding in the large set of available SLN data (Markov et al., 2014).

Given that the macaque SLN is correlated to the human DAI, we asked whether the human DAI also establishes a hierarchy of human visual areas, similar to the DAI-based hierarchy of macaque visual areas established previously (Bastos et al., 2015). Within each subject, we considered each area in turn as a seed area. The DAI values of this seed area relative to all areas were ranked (with the DAI of the seed to itself being zero, according to the DAI definition). Average ranking across all seven seed areas was established for each subject. Figure 7 shows average rankings and their SEMs across the 43 subjects. Figure 7A shows the rankings derived from the DAI in the

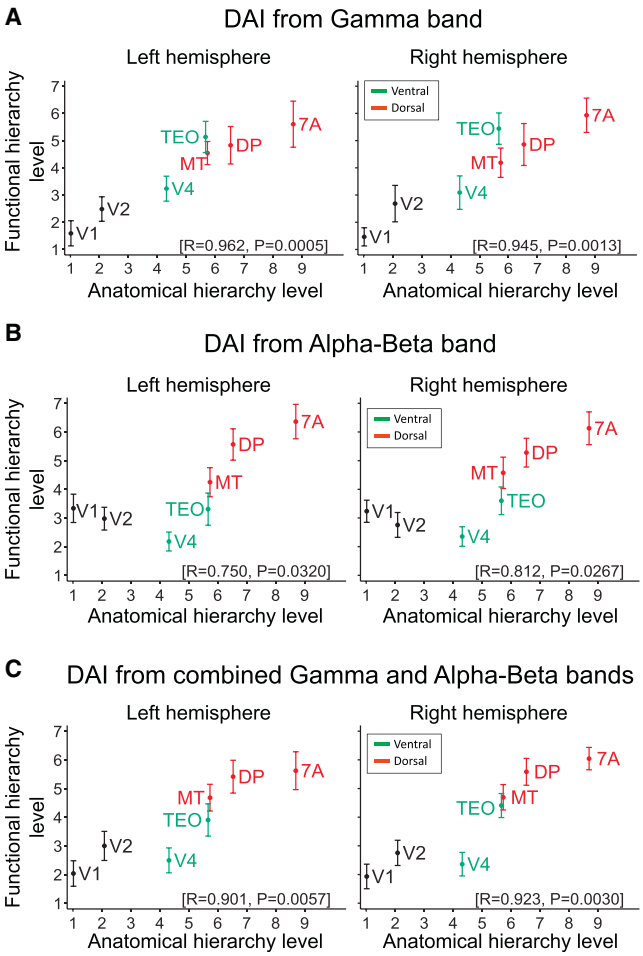

Figure 7. GC-Based Hierarchy Correlates with Anatomical Hierarchy

(A–C) The relation between the functional hierarchy of human visual areas and the anatomical hierarchy of homologous macaque areas was determined separately for the left and right hemispheres. The functional hierarchy of the human visual areas was computed from the DAI values (see Experimental Procedures). Three cases were investigated, namely, with the functional hierarchy computed from (A) DAI in the gamma band, (B) DAI in the alpha-beta band, and (C) the combined DAI in the alpha-beta and gamma bands. Early visual areas are depicted in black, ventral-stream areas in green, and dorsal-stream areas in red. Inset brackets on the bottom right of each subplot report Pearson correlation between human functional and macaque anatomical hierarchical levels. Notice the push toward lower hierarchical levels of midlevel ventral-stream areas by the inclusion of feedback causal influences in the alpha-beta band (compare C to A).

gamma-frequency band. The human GC-based ranking is plotted against the macaque anatomy-based ranking (Markov et al., 2014) and the two hierarchies are significantly correlated (left hemisphere: R = 0.962, p = 0.0005; right hemisphere: R = 0.945, p = 0.0013; Pearson correlations in this and the following tests). Note, an essentially perfect correlation existed for all areas, except TEO, which ranked slightly higher in the human GC-based than the macaque anatomy-based hierarchy. Note also that hierarchical levels span almost the entire possible range of seven levels, suggesting slightly less than seven levels as a first estimate of a lower bound for the number of hierarchical levels present in the data (see below for a higher estimate when more areas are included).

The same procedure was repeated with the DAI in the alpha-beta frequency band (after inverting its sign because of its negative correlation to SLN). The resulting relation to anatomy was less pronounced, because early visual areas V1 and V2 were placed higher and the ventral-stream areas V4 and TEO were placed lower than in the anatomical hierarchy (Figure 7B) (left hemisphere: R = 0.75, p = 0.032; right hemisphere: R = 0.812, p = 0.0267). A hierarchy based on average DAI values from both the gamma and the alpha-beta band (after inverting the latter) shows excellent correspondence between functional and anatomical hierarchies (Figure 7C) (left hemisphere: R = 0.901, p = 0.0057; right hemisphere: R = 0.923, p = 0.003). In comparison to the pure gamma-based hierarchy, the ventral-stream areas V4 and TEO are moved lower. This might be due to strong feedback influences exerted in the alpha-beta band (see Discussion).

Functional hierarchies built separately from the GC values in the two hemispheres were qualitatively identical (compare the two columns of Figure 7). Further, the results remained qualitatively unchanged when the analysis was repeated without alignment to the subject-wise peak frequencies in the alpha-beta and gamma band (Figure S3). When the analysis was repeated for areas randomly defined as contiguous patches of dipoles (with sizes similar to the actual areas), this produced correlations distributed around zero. All observed correlations exceeded the 97.5th percentile of these randomization distributions; i.e., they were significantly different in a two-sided test.

As an independent test for the presence of functional hierarchies, we computed repeated-measures one-way ANOVAs across subjects with the factor AREA and the dependent variable HIERARCHICAL LEVEL. The observed F-values were compared to the distribution of F-values from 1,000 trial shuffles. All hierarchies were highly significant (p values of 0–0.003).

GC Establishes a Functional Hierarchy across 26 Human Visual Areas

The analysis so far was limited to seven areas, for which the homology between human and macaque is well pronounced and for which quantitative retrograde tracing data were available. Given that the anatomical hierarchy was strongly correlated with a GC-based hierarchy, we next investigated whether a hierarchy can also be built for a larger set of human visual areas: V1, V2, V3, V3A, V3B, V3C, V3D, V4, V4t, LO1, LO2, PITd, PITv, MT, VO1, MST, FST, ER, V7, IPS1, IPS2, IPS3, IPS4, 7A, FEF, 46 (see Experimental Procedures for description). For these 26 areas, the functional hierarchical level was derived based on the DAI metric, in the same fashion as for the 7 areas. Figure 8A shows the 26 areas according to their functional hierarchical level. If the hierarchical ranking had not been consistent across seed areas within subjects, or across subjects, the different areas would rank roughly at the same hierarchical level. Similarly, if ranking were not consistent across subjects, the error bars would be large relative to the rank range. Thus, the fact that in Figure 8, the 26 areas span almost the entire dynamic range of

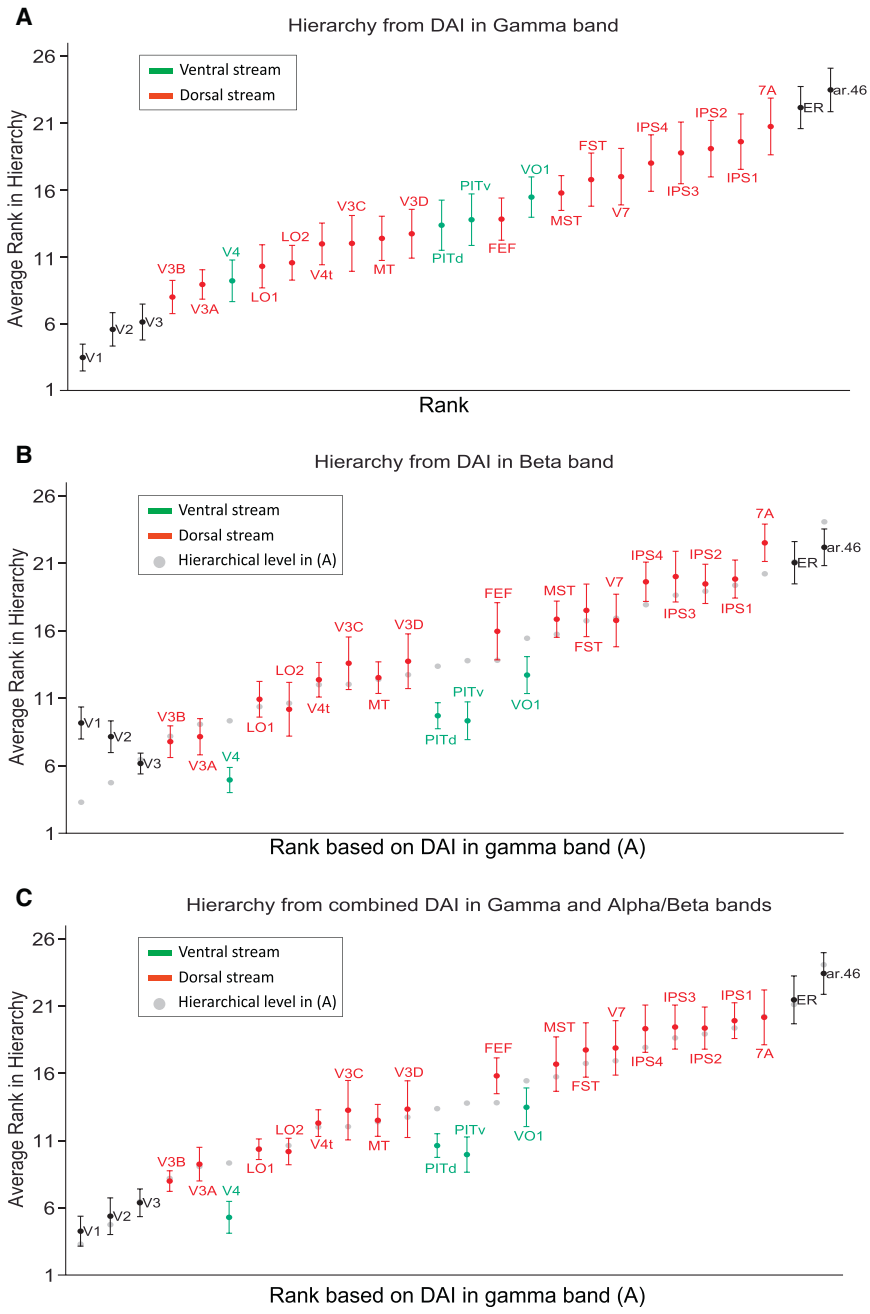

Figure 8. Functional Hierarchy of 26 Human Visual Areas

(A–C) The functional hierarchy of 26 human visual areas was computed based on (A) DAI in the gamma band, (B) DAI in the alpha-beta band, and (C) the combined DAI in the alpha-beta and gamma bands. The functional hierarchy in each case is the average of the functional hierarchies in the left and right hemispheres. Ventral-stream areas are depicted in green, dorsal-stream areas in red, and all other areas in black. In (A) the 26 areas have been ranked along the x axis based on their average hierarchical level depicted on the y axis. In (B) and (C), the ranking from (A) has been preserved on the x axis in order to illustrate changes in the hierarchy for DAIs of different frequency bands.

26 hierarchical levels, with relatively small error bars, suggests slightly less than 26 levels as a lower bound for the number of hierarchical levels present in the data. It also suggests that the organization of most area-pair-wise GC influences corresponds to a global hierarchy. In addition, the resulting hierarchy is in good agreement with the mosaic of evidence from different sources including quantitative anatomy (Barone et al., 2000; Markov et al., 2014), general anatomical connectivity and position (Felleman and Van Essen, 1991), and cognitive architectures (Dehaene et al., 2005). The location of the frontal eye field (FEF) low in the hierarchy is in agreement with recent quantitative analysis of retrograde tracing (Barone et al., 2000; Markov et al., 2014). In terms of hierarchical discriminability of areas, it is clear that areas are more separable at the upper and lower ends of the hierarchy than they are in the middle of the hierarchy.

The same procedure repeated in the alpha-beta band led to several areas changing their hierarchical level. To illustrate this, Figure 8B retains the x axis ordering established in Figure 8A on the basis of the gamma-band DAI but reports on the y axis the hierarchical level based on the alpha-beta band DAI (a copy of each area's gamma-DAI based hierarchical level is shown as a gray dot). In general, ventral-stream areas (labeled green) V4, PITv, PITd, and VO1 are moved to lower levels, whereas many dorsal-stream areas (labeled red) including V3C, V3D, MST, FST, IPS3, IPS4, and 7A are shifted to higher levels. Similarly, V1 and V2 are moved to higher levels. These shifts could be due to relatively strong alpha-beta-band influences exerted by the dorsal-stream areas onto the ventral-stream areas and exempting the earliest areas V1 and V2 (see Discussion). Likewise, FEF is shifted to a higher level, suggesting that it exerts relatively strong alpha-beta feedback.

The split between dorsal- and ventral-stream areas becomes even more apparent when the functional hierarchy is based on the DAIs from the gamma and alpha-beta bands combined (Figure 8C). Compared to a pure gamma-based hierarchy (gray dots), it shows a consistent upward shift for most dorsal-stream areas (V3C, V3D, MST, FST, V7, and IPS1–4) and a consistent downward shift for ventral-stream areas (V4, PITv, PITd, and VO1).

We repeated the ANOVA analysis for the 26 areas, and again all hierarchies were significant (p values ranging from 0 to 0.016).

DISCUSSION

We used MEG to study the spectral specificity of causal influences along inferred anatomical feedforward and feedback projections in the human visual cortex. Projections were defined as feedforward or feedback based on retrograde tracing data in homologous macaque visual areas. Frequency-resolved Granger causality between human visual cortical areas showed that causal influences along feedforward projections were predominant in the gamma band, whereas causal interactions along feedback projections were predominant in the alpha-beta band. Based on these results, we used all inter-areal GC values to build a functional hierarchy in human visual cortex, which was strongly correlated to the hierarchy derived from macaque retrograde tracing data. Finally, we extrapolated this to 26 human visual areas.

The present analyses are based on MEG data from 43 human subjects, which allowed us to use statistics that are non-parametric counterparts of random-effect statistics. The previous analysis using the electrocorticogram (ECoG) in macaques was restricted to two animals, as is typical for non-human primate studies, and thereby to a fixed-effect analysis. Whereas a fixed-effect analysis allows inference only on the tested sample, our present analysis allows generalization to the population of human subjects.

Fast Versus Slow Oscillations for Feedforward and Feedback Signaling

Several studies have reported that feedforward and feedback communication use respectively higher and lower frequency ranges. Some studies compared task conditions and found that conditions expected to emphasize feedforward signaling lead to stronger synchronization in relatively higher frequency bands, whereas conditions expected to emphasize feedback signaling lead to stronger synchronization in relatively lower frequency bands (von Stein et al., 2000; Buschman and Miller, 2007; Arnal et al., 2011). Other studies compared anatomical structures and found that pathways or layers involved in feedforward signaling show stronger synchronization at higher frequencies, and pathways or layers involved in feedback signaling show stronger synchronization in lower frequencies. For example, feedforward communication from medial entorhinal cortex to hippocampal area CA1 uses higher gamma, whereas feedback communication from CA3 to CA1 uses lower gamma (Colgin et al., 2009; Schomburg et al., 2014). In visual cortex, superficial layers, sending feedforward projections, show predominantly gamma-band synchronization, whereas infragranular layers, sending feedback projections, show predominantly alpha-beta-band synchronization (Buffalo et al., 2011; Xing et al., 2012). Across cortical sublayers, gamma shows phase shifts consistent with feedforward signaling (Livingstone, 1996; van Kerkoerle et al., 2014) and alpha shows phase shifts or GC consistent with feedback signaling (Bollimunta et al., 2011; van Kerkoerle et al., 2014). Direct quantification of directed influences by means of GC showed that inter-areal feedforward influences are carried by gamma and feedback influences by alpha or beta rhythms. Between human auditory area A1 and auditory association cortex, feedforward signaling uses gamma, and feedback signaling delta/beta rhythms (Fontolan et al., 2014). Between macaque visual areas V1 and V4, feedforward signaling uses gamma and feedback signaling alpha or beta (Bosman et al., 2012; van Kerkoerle et al., 2014).

Finally, a recent study investigated eight visual areas in macaque and found that across the numerous inter-areal projections, feedforward connectivity was systematically related to GC in the theta and gamma bands, and feedback connectivity was systematically related to GC in the beta band (Bastos et al., 2015). These earlier results from macaques agree fully with the present results for humans in the gamma band, but they agree only partly in the other frequency bands. Our present analysis in humans suggests that top-down influences are exerted by rhythms spanning alpha and beta frequency ranges, even though previous studies clearly suggest separate alpha and beta rhythms (Wang, 2010; Womelsdorf et al., 2014; Gregoriou et al., 2015). It is important to note that our analysis merely reveals whether directed influences in a frequency band relate to feedforward or feedback projections. Our results suggest that both alpha and beta subserve top-down signaling. Yet, this does not contradict differential mechanisms and sub-functions of top-down influences (Fries, 2015). Alpha might mediate top-down influences suppressing irrelevant background (van Kerkoerle et al., 2014), whereas beta might mediate top-down influences, that facilitate the bottom-up communication of attended stimuli (Lee et al., 2013; Bastos et al., 2015). Our present analysis did not reveal a convincing peak of GC influences in the theta frequency range, even though theta-band influences have been found in the earlier study with macaques (Bastos et al., 2015). The reason for this difference is currently unclear, and we can only speculate that it might be due to differences between ECoG and MEG or between the stimulus and/or task conditions.

Compared to infragranular connectivity, supragranular connectivity shows fine-grained spatial structure and interconnects some brain regions, such as, e.g., frontal cortex and ventral visual areas (Markov et al., 2014), possibly allowing frontal areas to change their functional hierarchical level dynamically (Bastos et al., 2015). In agreement with this, gamma-band GC influences between macaque FEF and V4 predominate in the FEF-to-V4 direction after an attentional cue, but subsequently predominate in the V4-to-FEF direction (Gregoriou et al., 2009). Between human frontal cortex and high-level ventral visual cortex, gamma-band coherence shows a 20 ms phase lead of frontal cortex (Baldauf and Desimone, 2014).

The present results, indicating a functional hierarchy of the human visual cortex, are relevant to future investigation of predictive coding in human cortex. Feedforward and feedback influences have been hypothesized to subserve the signaling of prediction errors and predictions, respectively. These concepts are central to the theory of predictive coding, stating in essence that higher areas constantly derive predictions based on incoming evidence and prior experience, and feed those predictions back to lower areas, where they are subtracted from sensory evidence, such that only prediction errors need to be forwarded to higher areas (Bastos et al., 2012). Crucially, in this framework, the updating of predictions entails the accumulation of prediction errors over time, so that predictions change

more slowly than prediction errors. Therefore, if predictions and prediction errors are mediated through inter-areal rhythmic synchronization, the communication of prediction errors requires higher frequencies than the communication of predictions. This is in agreement with several recent studies (Fontolan et al., 2014; van Kerkoerle et al., 2014; Bastos et al., 2015) and our finding that feedforward signaling is dominated by gamma and feedback signaling is dominated by alpha-beta rhythms.

Ventral-Stream Areas

Although the functional human hierarchy derived from the DAI was largely in agreement with the macaque anatomical hierarchy, some important deviations were observed, especially when the hierarchy was computed from the feedback causal asymmetries in the alpha-beta band. In this case, the ventral-stream areas V4 and TEO were much lower in the functional hierarchy than in the anatomical one. Feedback causal influences were strongest onto area V4 and progressively decreased toward the primary visual cortex. A similarly decreasing pattern has been observed for the effect of attention on firing rates in areas V1, V2, and V4 (Buffalo et al., 2010). In this work, a reverse order of attentional effects was shown, with a stronger and earlier enhancement in firing rates in V4 and progressively smaller and later enhancement in V2 and in V1. This strong feedback influence on V4 was also prominent in the hierarchy derived from the combined feedforward and feedback causal asymmetries as manifested in the unexpectedly low hierarchical position of V4 (at a similar level to V2).

These results suggest that feedback influences from higher ventral and dorsal areas primarily address mid-level ventral-stream areas such as V4 and TEO and to a lesser degree affect the earlier visual areas V2 and V1. It has already been suggested that early ventral-stream areas, and especially area V4, are well positioned for integrating top-down influences with bottom-up information (Roe et al., 2012), mainly due to strong corticocortical (Cloutman, 2013; Markov et al., 2014) and corticothalamocortical (Van Essen, 2005) anatomical connections with temporal, prefrontal, and parietal regions.

Also, details of the task may differentially impact the patterns of alpha-beta band top-down influences. Our task required subjects to detect a speed change in a drifting grating and may therefore predominantly engage the dorsal stream. It is conceivable that this contributed to strong alpha-beta band influences from dorsal- to ventral-stream areas, which in turn places dorsal-stream areas higher and ventral-stream areas lower in the functional hierarchy. Future studies might systematically investigate changes in the functional hierarchy as a function of task requirements.

Functional Hierarchy of 26 Visual Areas

Using the asymmetry in causal interactions, we estimated the functional hierarchy for 26 areas of the human visual system. For several of the 26 areas, it is not possible to establish a clear homology to areas in the non-human primate brain. Yet, for the areas for which a homology can be hypothesized, there was a good agreement between functional and anatomical hierarchical level (Felleman and Van Essen, 1991; Markov et al., 2014). Furthermore, for areas defined only in humans, the functional hierarchical level agreed with expectations derived from the overall position in the brain and functional characteristics. The strong effect of feedback causal influences on mid-level ventral-stream areas was observed also in this hierarchy.

EXPERIMENTAL PROCEDURES

Experimental Paradigm

The experimental paradigm (Figure 1A) was adopted from (van Pelt et al., 2012) and (Hoogenboom et al., 2006) and is known to induce strong gamma band oscillations in occipital areas. Each trial was initiated with a fixation point (Gaussian of diameter 0.5 deg.) at the center of the screen for 1.5 s. The fixation period was followed by the presentation of a circular sine-wave grating, centered at the fixation point and contracting toward its center (spatial frequency: 3 cycles/deg, velocity: 0.66 deg/s, contrast: 100%). The screen background was black. At a random moment between 0.75 and 3 s after stimulus onset, the velocity increased (step to 1 deg/s), which was reported by the subjects with their right index finger. After the response followed a rest period of 1 s, during which feedback was given. A total of 180 trials were presented to each subject. Visual presentation was performed on a translucent screen, situated 0.9 m in front of subjects' eyes by using an LCD projector with a 60-Hz update rate. We quantified the MEG signal components locked to the LCD update for sensors over the visual cortex (Figure 1C), and we found them to account for a very small part of the total power at 60 Hz (< 1.94% of 60 Hz power during baseline, < 1.42% of 60 Hz power during stimulation). Note that data were acquired in Europe; i.e., the power line frequency was 50 Hz.

Data Acquisition

MEG: Recordings were performed with a whole-head MEG system (CTF Systems) comprising 275 axial gradiometers. MRI: Structural MR images were acquired using an Avanto 1.5 T whole-body MRI scanner (Siemens, Germany). Further details can be found in the corresponding section of Supplemental Experimental Procedures.

Subjects

Datasets of 43 subjects were selected from a pool of 160 subjects, which had been recorded for genotyping of parameters derived from visually induced gamma-band activity. Further details on selection criteria can be found in the corresponding section of Supplemental Experimental Procedures. All subjects gave written informed consent according to guidelines of the local ethics committee (Commissie Mensgebonden Onderzoek Regio Arnhem-Nijmegen, the Netherlands).

Data Preprocessing and Spectral Estimation

All MEG data analysis was performed in MATLAB, partly using the FieldTrip toolbox (Oostenveld et al., 2011). Data segments that contained artifacts originating from jumps in the SQUIDs (super-conducting quantum interference devices), muscle activity and eye movements were identified and removed using semi-automated FieldTrip routines. Power-line artifacts were estimated and removed using a discrete Fourier transform at 50, 100 and 150 Hz with a bin width of ± 0.25 Hz. We used data from 0.365 s after stimulus onset until the visual stimulus changed speed, thereby excluding stimulus-onset or stimulus–change-related non-stationarities. These data were divided into non-overlapping 0.365-s epochs. This fixed epoch length provided a good compromise between optimizing the use of the variable-length trials and maximizing the spectral resolution for the non-parametric spectral factorization employed in the calculation of GC. Epochs taken from early or late in the trial (median split) did not differ in their GC and were therefore pooled. Spectral estimation was first performed at the sensor level. Per sensor, each data epoch was demeaned, Hann-tapered, zero-padded to 1 s length, and Fourier transformed to give a spectrum between 1 and 140 Hz (Percival and Walden, 2000).

Human Brain Model

For source analysis, structural MR images were acquired for each individual subject and the cortical mantle was extracted with the FreeSurfer longitudinal-stream pipeline (Reuter et al., 2012). Cortical parcellation and area

definition used a recent visuotopic atlas provided by (Abdollahi et al., 2014), the FreeSurfer software suite (http://FreeSurfer.net/) (Fischl et al., 2004; Desikan et al., 2006; Destrieux et al., 2010), and the Caret software suite (http://brainvis.wustl.edu/) (Glasser and Van Essen, 2011; Van Essen et al., 2012).

Further details on the construction of the source space with the investigated visual areas can be found in the corresponding section of Supplemental Experimental Procedures.

Selection of Homologous Brain Areas between Human and Macaque

We aimed at relating functional connectivity derived from human MEG recordings to anatomical connectivity derived from macaque retrograde tracing experiments. Therefore, the availability of retrograde tract tracing data dictated the selection of visual areas. From the set of areas in the occipital, parietal, and temporal cortical regions with such tracing data, a subset was selected for which evidence of homology between human and macaque brains exists in the literature. These areas were V1, V2, MT, V4, DP, TEO, and 7A and are shown in Figure 2B. The numbers of dipoles per area are listed in Table S1.

More details about the selected areas and their homology between species can be found in the corresponding section of Supplemental Experimental Procedures.

Parcels representing areas V1 and V2 are quite extensive in comparison to the other parcels and contain a large number of voxels that are far from the main locus of activation, as defined by visually induced gamma power enhancement (Figure 2). In order to minimize the effect of the resulting extensive smoothing, a more spatially confined representation for these areas has been employed. In this representation, V1 and V2 parcels consist of the vertices within 2 cm from the local gamma power maxima within the original representation of these areas.

Inverse Solution

Subject-wise structural MRI scans were used to derive individual single-shell volume conductor models (Nolte, 2003). The inverse solution was then performed using linearly constrained minimum variance (LCMV) adaptive spatial filtering, often referred to as "beamforming." When determining the LCMV solution, we used a regularization parameter of 20% of the covariance matrix.

For further details on the inverse solution, please see the corresponding section in Supplemental Experimental Procedures.

GC

In order to study the strength and directionality of causal influences between the investigated brain areas, we employed GC (Granger, 1969), a statistical measure that quantifies the extent to which one time series can predict another. The principal idea behind GC is that if the addition of the history of signal A improves the prediction of signal B, as compared to the prediction of signal B based on its own history alone, then signal A is said to "Granger-cause" signal B.

This measure of predictive causality can be estimated either in the time domain or in the frequency domain (Geweke, 1982). In the latter case, GC provides a spectrum of causal interactions between the two signals as a function of frequency. This is of great utility for the analysis of MEG data because oscillations at distinct frequencies can be simultaneously realized in different brain areas and likely subserve inter-areal communication (Fries, 2005, 2015). GC can be calculated using parametric methods based on multivariate autoregressive models. This approach requires the selection of model parameters and can fail to capture complex spectral features (Mitra and Pesaran, 1999). Therefore, we used a non-parametric approach, which estimates GC directly from a factorization of the cross-spectral density (CSD) matrix (Dhamala et al., 2008). For the present study, the CSD of two brain sources is simply the scalar product between their complex and complex-conjugate spectral coefficient sequences. These coefficients are computed by multiplying the sensor-level spectral decomposition with the spatial filter for each location.

The visuotopic source space used in this work consists of the set of points distributed within the brain areas of interest, referred to as "parcels." To calculate the GC between two parcels, we first averaged the CSD between all inter-parcel dipole pairs. Within parcels, the power spectral density was computed by averaging all the within-parcel power-spectral density values.

Retrograde Tracing Database

A description of the anatomical dataset acquisition and analysis has been reported in Markov et al. (2014). Please see also the Supplemental Experimental Procedures for additional information.

Selection of 26 Visual Areas from the Human Brain

For this analysis, we extended the initial set of 7 visual areas, for which anatomical connectivity information was available, to an extended set of 26 areas involved in visual processing. The additional areas were V3, V3A, V3B, V3C, V3D, V4t, LO1, LO2, VO1, MST, and FST from the atlas of Abdollahi et al. (2014) and areas IPS1, IPS2, IPS3, IPS4, 46, ER from the visuotopic atlas of Caret (Van Essen et al., 2012). Area PIT from the 7-area analysis was split into its two constituent areas PITv, PITd from the atlas of Abdollahi et al. (2014). FEFs were manually selected. For further details on the 26 selected visual areas, see the Supplemental Experimental Procedures.

Statistical Testing

Figures 4 and 5 use randomization-based non-parametric statistical tests with cluster-based multiple comparison correction (Maris and Oostenveld, 2007). Each subject provided one feedforward and one feedback GC spectrum, which were compared across subjects via t tests. The t-values of spectrally adjacent, significant t tests were summed to generate the observed (first-level, cluster-based) test metric (not used for inference). We then performed 1000 randomizations. In each randomization, feedforward and feedback labels were randomly exchanged per subject, and the test metric was computed as for the non-randomized data. Per randomization, the largest test metric was entered into the randomization distribution. The observed test metrics were compared against the randomization distribution. Comparisons between feedforward or feedback GC versus the bias estimates proceeded accordingly. Similarly, the correlation coefficients between DAI and SLN values (computed as explained in the Results section) were tested against zero (Figure 6) and against bias estimates (Figure S2); i.e., each subject provided one correlation spectrum and either one null spectrum or one bias-estimate spectrum.

SUPPLEMENTAL INFORMATION

Supplemental Information includes Supplemental Experimental Procedures, three figures, and one table and can be found with this article online at http://dx.doi.org/10.1016/j.neuron.2015.12.018.

AUTHOR CONTRIBUTIONS

Conceptualization, G.M., J.V., and P.F.; Methodology, G.M., J.V., and J.S.; Formal Analysis, G.M. and J.V.; Investigation, S.P. and H.K.; Resources, P.F.; Writing – Original Draft, G.M. and P.F.; Writing – Review & Editing, G.M., J.V., S.P., J.S., H.K., and P.F.; Visualization, G.M.; Supervision, P.F.; Project Administration, P.F.; Funding Acquisition, P.F.

ACKNOWLEDGMENTS

We thank Marieke van de Nieuwenhuijzen for assisting in the recording of MEG datasets and Eric Maris for help with non-parametric statistics. This work was supported by the Human Connectome Project (WU-Minn Consortium, NIH grant 1U54MH091657 to P.F.), a European Young Investigator Award (P.F.), the European Union (HEALTH-F2-2008-200728 to P.F.), the LOEWE program ("Neuronale Koordination Forschungsschwerpunkt Frankfurt" to P.F.), NWO (VIDI grant to J.S.), the Smart Mix Program of the Netherlands Ministry of Economic Affairs and the Netherlands Ministry of Education, Culture and Science (BrainGain to P.F. and J.S.), ANR-11-BSV4-501 (H.K.), and LabEx CORTEX (ANR-11-LABX-0042 to H.K.).

Received: June 5, 2015
Revised: November 6, 2015
Accepted: December 8, 2015
Published: January 14, 2016

REFERENCES

Abdollahi, R.O., Kolster, H., Glasser, M.F., Robinson, E.C., Coalson, T.S., Dierker, D., Jenkinson, M., Van Essen, D.C., and Orban, G.A. (2014). Correspondences between retinotopic areas and myelin maps in human visual cortex. Neuroimage *99*, 509–524.

Arnal, L.H., Wyart, V., and Giraud, A.-L. (2011). Transitions in neural oscillations reflect prediction errors generated in audiovisual speech. Nat. Neurosci. *14*, 797–801.

Baldauf, D., and Desimone, R. (2014). Neural mechanisms of object-based attention. Science *344*, 424–427.

Barone, P., Batardiere, A., Knoblauch, K., and Kennedy, H. (2000). Laminar distribution of neurons in extrastriate areas projecting to visual areas V1 and V4 correlates with the hierarchical rank and indicates the operation of a distance rule. J. Neurosci. *20*, 3263–3281.

Bastos, A.M., Usrey, W.M., Adams, R.A., Mangun, G.R., Fries, P., and Friston, K.J. (2012). Canonical microcircuits for predictive coding. Neuron *76*, 695–711.

Bastos, A.M., Vezoli, J., Bosman, C.A., Schoffelen, J.-M., Oostenveld, R., Dowdall, J.R., De Weerd, P., Kennedy, H., and Fries, P. (2015). Visual areas exert feedforward and feedback influences through distinct frequency channels. Neuron *85*, 390–401.

Bollimunta, A., Chen, Y., Schroeder, C.E., and Ding, M. (2008). Neuronal mechanisms of cortical alpha oscillations in awake-behaving macaques. J. Neurosci. *28*, 9976–9988.

Bollimunta, A., Mo, J., Schroeder, C.E., and Ding, M. (2011). Neuronal mechanisms and attentional modulation of corticothalamic α oscillations. J. Neurosci. *31*, 4935–4943.

Bosman, C.A., Schoffelen, J.-M., Brunet, N., Oostenveld, R., Bastos, A.M., Womelsdorf, T., Rubehn, B., Stieglitz, T., De Weerd, P., and Fries, P. (2012). Attentional stimulus selection through selective synchronization between monkey visual areas. Neuron *75*, 875–888.

Bressler, S.L., and Richter, C.G. (2015). Interareal oscillatory synchronization in top-down neocortical processing. Curr. Opin. Neurobiol. *31*, 62–66.

Buffalo, E.A., Fries, P., Landman, R., Liang, H., and Desimone, R. (2010). A backward progression of attentional effects in the ventral stream. Proc. Natl. Acad. Sci. USA *107*, 361–365.

Buffalo, E.A., Fries, P., Landman, R., Buschman, T.J., and Desimone, R. (2011). Laminar differences in gamma and alpha coherence in the ventral stream. Proc. Natl. Acad. Sci. USA *108*, 11262–11267.

Buschman, T.J., and Miller, E.K. (2007). Top-down versus bottom-up control of attention in the prefrontal and posterior parietal cortices. Science *315*, 1860–1862.

Cloutman, L.L. (2013). Interaction between dorsal and ventral processing streams: where, when and how? Brain Lang. *127*, 251–263.

Colgin, L.L., Denninger, T., Fyhn, M., Hafting, T., Bonnevie, T., Jensen, O., Moser, M.B., and Moser, E.I. (2009). Frequency of gamma oscillations routes flow of information in the hippocampus. Nature *462*, 353–357.

Dehaene, S., Duhamel, J.R., Hauser, M.D., and Rizzolatti, G. (2005). From Monkey Brain to Human Brain: A Fyssen Foundation Symposium (Cambridge, MA: MIT Press).

Desikan, R.S., Ségonne, F., Fischl, B., Quinn, B.T., Dickerson, B.C., Blacker, D., Buckner, R.L., Dale, A.M., Maguire, R.P., Hyman, B.T., et al. (2006). An automated labeling system for subdividing the human cerebral cortex on MRI scans into gyral based regions of interest. Neuroimage *31*, 968–980.

Destrieux, C., Fischl, B., Dale, A., and Halgren, E. (2010). Automatic parcellation of human cortical gyri and sulci using standard anatomical nomenclature. Neuroimage *53*, 1–15.

Dhamala, M., Rangarajan, G., and Ding, M. (2008). Estimating Granger causality from Fourier and wavelet transforms of time series data. Phys. Rev. Lett. *100*, 018701.

Felleman, D.J., and Van Essen, D.C. (1991). Distributed hierarchical processing in the primate cerebral cortex. Cereb. Cortex *1*, 1–47.

Fischl, B., van der Kouwe, A., Destrieux, C., Halgren, E., Ségonne, F., Salat, D.H., Busa, E., Seidman, L.J., Goldstein, J., Kennedy, D., et al. (2004). Automatically parcellating the human cerebral cortex. Cereb. Cortex *14*, 11–22.

Fontolan, L., Morillon, B., Liegeois-Chauvel, C., and Giraud, A.-L. (2014). The contribution of frequency-specific activity to hierarchical information processing in the human auditory cortex. Nat. Commun. *5*, 4694–4694.

Fries, P. (2005). A mechanism for cognitive dynamics: neuronal communication through neuronal coherence. Trends Cogn. Sci. *9*, 474–480.

Fries, P. (2015). Rhythms for cognition: Communication through coherence. Neuron *88*, 220–235.

Geweke, J. (1982). Measurement of linear dependence and feedback between multiple time series. J. Am. Stat. Assoc. *77*, 304–313.

Glasser, M.F., and Van Essen, D.C. (2011). Mapping human cortical areas in vivo based on myelin content as revealed by T1- and T2-weighted MRI. J. Neurosci. *31*, 11597–11616.

Granger, C.W.J. (1969). Investigating causal relations by econometric models and cross-spectral methods. Econometrica *37*, 424–438.

Gregoriou, G.G., Gotts, S.J., Zhou, H., and Desimone, R. (2009). High-frequency, long-range coupling between prefrontal and visual cortex during attention. Science *324*, 1207–1210.

Gregoriou, G.G., Paneri, S., and Sapountzis, P. (2015). Oscillatory synchrony as a mechanism of attentional processing. Brain Res. *1626*, 165–182.

Haegens, S., Cousijn, H., Wallis, G., Harrison, P.J., and Nobre, A.C. (2014). Inter- and intra-individual variability in alpha peak frequency. Neuroimage *92*, 46–55.

Hoogenboom, N., Schoffelen, J.-M., Oostenveld, R., Parkes, L.M., and Fries, P. (2006). Localizing human visual gamma-band activity in frequency, time and space. Neuroimage *29*, 764–773.

Jutai, J.W., Gruzelier, J.H., and Connolly, J.F. (1984). Spectral analysis of the visual evoked potential (VEP): effects of stimulus luminance. Psychophysiology *21*, 665–672.

Lee, J.H., Whittington, M.A., and Kopell, N.J. (2013). Top-down beta rhythms support selective attention via interlaminar interaction: a model. PLoS Comput. Biol. *9*, e1003164.

Livingstone, M.S. (1996). Oscillatory firing and interneuronal correlations in squirrel monkey striate cortex. J. Neurophysiol. *75*, 2467–2485.

Maris, E., and Oostenveld, R. (2007). Nonparametric statistical testing of EEG- and MEG-data. J. Neurosci. Methods *164*, 177–190.

Markov, N.T., Vezoli, J., Chameau, P., Falchier, A., Quilodran, R., Huissoud, C., Lamy, C., Misery, P., Giroud, P., Ullman, S., et al. (2014). Anatomy of hierarchy: feedforward and feedback pathways in macaque visual cortex. J. Comp. Neurol. *522*, 225–259.

Mitra, P.P., and Pesaran, B. (1999). Analysis of dynamic brain imaging data. Biophys. J. *76*, 691–708.

Muckli, L., De Martino, F., Vizioli, L., Petro, L.S., Smith, F.W., Ugurbil, K., Goebel, R., and Yacoub, E. (2015). Contextual Feedback to Superficial Layers of V1. Curr. Biol. *25*, 2690–2695.

Nolte, G. (2003). The magnetic lead field theorem in the quasi-static approximation and its use for magnetoencephalography forward calculation in realistic volume conductors. Phys. Med. Biol. *48*, 3637.

Olman, C.A., Harel, N., Feinberg, D.A., He, S., Zhang, P., Ugurbil, K., and Yacoub, E. (2012). Layer-specific fMRI reflects different neuronal computations at different depths in human V1. PLoS ONE *7*, e32536.

Oostenveld, R., Fries, P., Maris, E., and Schoffelen, J.-M. (2011). FieldTrip: Open source software for advanced analysis of MEG, EEG, and invasive electrophysiological data. Comput. Intell. Neurosci. *2011*, 156869.

Percival, D.B., and Walden, A.T. (2000). Wavelet Methods for Time Series Analysis (Cambridge Series in Statistical and Probabilistic Mathematics) (Cambridge University Press).

Plomp, G., Quairiaux, C., Kiss, J.Z., Astolfi, L., and Michel, C.M. (2014). Dynamic connectivity among cortical layers in local and large-scale sensory processing. Eur. J. Neurosci. *40*, 3215–3223.

Reuter, M., Schmansky, N.J., Rosas, H.D., and Fischl, B. (2012). Within-subject template estimation for unbiased longitudinal image analysis. Neuroimage *61*, 1402–1418.

Roe, A.W., Chelazzi, L., Connor, C.E., Conway, B.R., Fujita, I., Gallant, J.L., Lu, H., and Vanduffel, W. (2012). Toward a unified theory of visual area V4. Neuron *74*, 12–29.

Salin, P.A., and Bullier, J. (1995). Corticocortical connections in the visual system: structure and function. Physiol. Rev. *75*, 107–154.

Schoffelen, J.-M., and Gross, J. (2009). Source connectivity analysis with MEG and EEG. Hum. Brain Mapp. *30*, 1857–1865.

Schomburg, E.W., Fernández-Ruiz, A., Mizuseki, K., Berényi, A., Anastassiou, C.A., Koch, C., and Buzsáki, G. (2014). Theta phase segregation of input-specific gamma patterns in entorhinal-hippocampal networks. Neuron *84*, 470–485.

Sethian, J.A. (1999). Level Set Methods and Fast Marching Methods: Evolving Interfaces in Computational Geometry, Fluid Mechanics, Computer Vision, and Materials Science (Cambridge University Press).

Van Essen, D.C. (2005). Corticocortical and thalamocortical information flow in the primate visual system. Prog. Brain Res. *149*, 173–185.

Van Essen, D.C., Glasser, M.F., Dierker, D.L., Harwell, J., and Coalson, T. (2012). Parcellations and hemispheric asymmetries of human cerebral cortex analyzed on surface-based atlases. Cereb. Cortex *22*, 2241–2262.

van Kerkoerle, T., Self, M.W., Dagnino, B., Gariel-Mathis, M.-A., Poort, J., van der Togt, C., and Roelfsema, P.R. (2014). Alpha and gamma oscillations characterize feedback and feedforward processing in monkey visual cortex. Proc. Natl. Acad. Sci. USA *111*, 14332–14341.

van Pelt, S., Boomsma, D.I., and Fries, P. (2012). Magnetoencephalography in twins reveals a strong genetic determination of the peak frequency of visually induced γ-band synchronization. J. Neurosci. *32*, 3388–3392.

von Stein, A., Chiang, C., and König, P. (2000). Top-down processing mediated by interareal synchronization. Proc. Natl. Acad. Sci. USA *97*, 14748–14753.

Wang, X.-J. (2010). Neurophysiological and computational principles of cortical rhythms in cognition. Physiol. Rev. *90*, 1195–1268.

Wang, X., Chen, Y., and Ding, M. (2008). Estimating Granger causality after stimulus onset: a cautionary note. Neuroimage *41*, 767–776.

Womelsdorf, T., Valiante, T.A., Sahin, N.T., Miller, K.J., and Tiesinga, P. (2014). Dynamic circuit motifs underlying rhythmic gain control, gating and integration. Nat. Neurosci. *17*, 1031–1039.

Xing, D., Yeh, C.-I., Burns, S., and Shapley, R.M. (2012). Laminar analysis of visually evoked activity in the primary visual cortex. Proc. Natl. Acad. Sci. USA *109*, 13871–13876.